Fiber neutrality in fiber-reinforced composites
Evidence from a computational study

Goudarzi, M.; Simone, A.

DOI
10.1016/j.ijsolstr.2018.07.023

Publication date
2019

Document Version
Final published version

Published in
International Journal of Solids and Structures

International Journal of Solids and Structures 156–157 (2019) 14–28

Contents lists available at ScienceDirect

International Journal of Solids and Structures

journal homepage: www.elsevier.com/locate/ijsolstr

Fiber neutrality in fiber-reinforced composites: Evidence from a computational study

M. Goudarzi[a,*], A. Simone[a,b]

[a] Faculty of Civil Engineering and Geosciences, Delft University of Technology, Delft, the Netherlands
[b] Department of Industrial Engineering, University of Padova, Padua, Italy

ARTICLE INFO

Article history:
Received 1 February 2018
Revised 29 May 2018
Available online 1 August 2018

Keywords:
Fiber-reinforced composites
Embedded reinforcement
Fiber neutrality

ABSTRACT

We report numerical evidence for neutrality of thin fibers to a prescribed uniform stress field in a fiber-reinforced composite. Elastic finite element analyses of fiber-reinforced composites are carried out with a conventional fully-resolved model and a novel dimensionally-reduced fiber model.The two modeling approaches are compared in the analysis of mechanical properties and matrix-fiber slip profiles. An analysis of the effectiveness of various fiber orientations with respect to the loading direction shows that the notion of inclusion neutrality, originally formulated for rigid line inclusions by Wang et al. [Journal of Applied Mechanics, 52(4), 814–822, 1985], holds also for linear elastic thin fibers with imperfect interface.

1. Introduction

Apart from fiber shape, surface treatment, and volume fraction, fiber spatial orientation is an important characteristic controlling load-transmission mechanisms in fiber-reinforced composites (Kang and Gao, 2002). Although the effect of fiber orientation can be accurately assessed by means of computational homogenization techniques (Berger et al., 2005; Xia et al., 2003; Mortazavi et al., 2013; Sheng et al., 2004; Lusti and Gusev, 2004), the generation of a conformal finite element mesh for composites with thin fibers is a tedious and time-consuming task. Embedded reinforcement techniques, in which fiber discretization is independent from the discretization of the composite domain, can be effectively used for this class of problems. Here we assess the validity of a novel embedded formulation and employ it to show inherent characteristics of composites reinforced with thin fibers.

Generally speaking, two classes of methods are available for the micro-mechanical study of fiber-reinforced composites: mean-field and direct numerical methods. Although mean-field methods such as Eshelby-based two-step homogenization schemes (Pierard et al., 2004; Tian et al., 2016) are fast and cost-effective, finite element (FE) averaging methods have gained popularity for their accurate geometrical representation of the composite micro-structure. A serious drawback of classical FE-based homogenization is the conformal mesh generation process for composites with many fibers. When the number of fibers is relatively low, the composite can still be discretized using classical conformal approaches as shown by Lusti and Gusev (2004) and Tian et al. (2016): in Lusti and Gusev (2004, Fig. 1) the discretization for a composite with 350 nanotubes of aspect ratio 200 at a volume fraction of 0.5% consists of 3.5×10^6 nodes tessellated into 21×10^6 tetrahedral elements; in Tian et al. (2016), the authors show that they can generate a discretization for a composite fiber volume fractions up to 20% considering 600 fibers (using therefore fibers with a relatively large diameter). Obviously, the study of composites with thousands or tens of thousands of fibers with volume fractions around 20% (typical of nanocomposites Andrews et al. (2002)) would be unfeasible with conformal approaches. Advanced discretization approaches such as embedded reinforcement methods (Balakrishnan and Murray, 1986; Elwi and Hrudey, 1989; Hartl, 2002; Barzegar and Maddipudi, 1997; Ninić et al., 2014; Radtke et al., 2010) facilitate the discretization of high aspect ratio fibers by allowing their mesh-independent representation. In the literature, these methods have been applied to curved inclusions (Elwi and Hrudey, 1989), sliding fibers (Barzegar and Maddipudi, 1997; Hartl, 2002; Radtke et al., 2010), and to describe the interaction between pile foundations and the surrounding soil (Ninić et al., 2014). In the simula-

* Corresponding author.
E-mail addresses: m.goudarzi@tudelft.nl (M. Goudarzi), angelo.simone@unipd.it, a.simone@tudelft.nl (A. Simone).

https://doi.org/10.1016/j.ijsolstr.2018.07.023

tion in Section 5 we have used up to around 22000 fibers with relatively coarse discretizations.

To lift the conformal meshing requirements of standard FE methods, two key assumptions are made in embedded formulations: (i) high aspect ratio fibers are described as one-dimensional bar or beam elements; and (ii) the fiber kinematics is introduced by means of a displacement gap between matrix and fiber while preserving the continuity of the underlying matrix displacement field across the fiber. Relaxing the second assumption in an embedded formulation requires the use of special enriched approximations (Pike and Oskay, 2016) that would significantly reduce the cost-effectiveness of the method and increase its complexity. For the analysis of composites with many fibers we prefer to adopt the most convenient approach from the computational point of view. In Section 2 we therefore propose a novel embedded reinforced technique, which is compared to a fully-resolved three-dimensional fiber-reinforced model in Section 3. The numerical formulation proposed in this paper is superior to existing embedded reinforcement models in that it uses totally independent finite element meshes for fiber and matrix. This will eliminate the need for calculating intersections between fiber and matrix elements, which may require complex algorithms especially for curved fibers (Durand et al., 2015). Even if the computational setup is very simple, the one-to-one comparison between a fully-resolved and a dimensionally-reduced fiber model allows us to assess the accuracy of the dimensionally-reduced model in terms of global (homogenized effective stiffness) and local (matrix-fiber slip profiles) quantities. To the author's knowledge, this type of comparison has not been reported in previous studies and validates the use of dimensionally-reduced models for fibers with sufficiently small diameters.

Numerical homogenization studies of fiber orientation effects (Tian et al., 2016; 2014; Kang and Gao, 2002) show that the composite stiffness is very sensitive to fiber misalignments. In a numerical study, Tian et al. (2016, Fig. 7b) showed that the effective Young's modulus along the loading direction in a carbon fiber composite decreases rather quickly when the fibers are misaligned with respect to the loading direction and reaches its minimum value, with a decrease of $\approx$25% from its maximum, when the fibers are inclined at 60° to the loading direction. Although the authors did not establish a correlation between elastic properties and geometrical properties such as fiber orientation and diameter, their results can be related, mutatis mutandis, to those obtained for zero-thickness rigid inclusions (or rigid line inclusions, RLIs) problems (Wang et al., 1985). In RLI problems, the solution fields show a strong dependence on the inclusion orientation and matrix Poisson's contraction effects, with the limit case of the inclusion being neutral (this, e.g., means that the stress field is not perturbed for certain inclusion orientations). In the literature, inclusion neutrality has been demonstrated only for perfectly bonded RLIs and for in-plane states in experiments (Noselli et al., 2010), theoretical studies (Wang et al., 1985; Dal Corso et al., 2016), and simulations (Barbieri and Pugno, 2015). In this contribution we demonstrate for the first time the validity of the concept of inclusion neutrality for high aspect ratio fibers in a three-dimensional volume. In Section 4, we show various forms of inclusion neutrality in a fiber-reinforced composite with linear elastic thin fibers with perfect and imperfect matrix-fiber interface using fully-resolved and dimensionally-reduced fiber models. Results are reported in terms of Young's moduli, shear moduli and Poisson's ratios. To demonstrate the applicability of the dimensionally-reduced model to composites with many fibers, Section 5 reports a detailed micromechanical study. Results, including some observations on fiber neutrality with respect to the effective Poisson's ratio of the composite, are compared with rule-of-mixtures predictions, while the limitations of the latter are pointed out.

2. Method

2.1. Weak form of the governing equations

With reference to the principle of virtual work for a small displacement elastostatics problem, the weak form of the governing equations for a fiber-reinforced composite without body forces is

$$\int_{\Omega_\mathrm{m}} \boldsymbol{\sigma}_\mathrm{m} : \nabla^\mathrm{s}\delta\boldsymbol{u}_\mathrm{m}\,\mathrm{d}\Omega_\mathrm{m} + \int_{\Omega_\mathrm{f}} \boldsymbol{\sigma}_\mathrm{f} : \nabla^\mathrm{s}\delta\boldsymbol{u}_\mathrm{f}\,\mathrm{d}\Omega_\mathrm{f} + \int_{\Gamma_\mathrm{int}} \boldsymbol{t}_\mathrm{c}\cdot\delta\boldsymbol{w}\,\mathrm{d}\Gamma_\mathrm{int} - \int_{\Gamma_\mathrm{t}} \bar{\boldsymbol{t}}\cdot\delta\boldsymbol{u}_\mathrm{m}\,\mathrm{d}\Gamma_\mathrm{t} = 0, \tag{1}$$

where ∇^s is the symmetric-gradient operator, and the integral over the total volume $\Omega = \Omega_\mathrm{m} \cup \Omega_\mathrm{f}$ is subdivided into matrix and fiber contributions. The virtual displacement vectors $\delta\boldsymbol{u}_\mathrm{m}$ and $\delta\boldsymbol{u}_\mathrm{f}$ and the corresponding stress tensors $\boldsymbol{\sigma}_\mathrm{m}$ and $\boldsymbol{\sigma}_\mathrm{f}$ are defined over matrix (m) and fiber (f) regions. The contribution along the matrix-fiber interface Γ_int represents the virtual mechanical work done by the interface tractions $\boldsymbol{t}_c$ for the local virtual opening (sliding) vector $\delta\boldsymbol{w}$ across (between) the two sides of the interface. The interface integral is evaluated over the interface surface Γ_int of the embedded fibers and, for convenience, is expressed in a coordinate system local to each fiber. The last term in (1) is the work done by the external tractions $\bar{\boldsymbol{t}}$ over the external surface Γ_t.

2.2. Discretized weak form

In the context of the finite element method, the domain Ω is discretized into matrix and fiber finite elements, each with its own set of degrees of freedom. To introduce fiber and matrix-fiber interface contributions (second and third terms in (1)), reference is made to two fiber discretizations: a conformal approach and a mesh-independent approach. While the approximation of the fiber displacement vector $\boldsymbol{u}_\mathrm{f}$ and the opening/sliding vector $\boldsymbol{w}$, later referred to as the interface gap vector, is specific to each scheme, the final discretized form of the governing equations is very similar for both techniques. Next, the discretization of matrix, fiber, and matrix-fiber interface is discussed in detail.

2.2.1. Matrix

The matrix displacement field $\boldsymbol{u}_\mathrm{m}$ is approximated at the element level as

$$\boldsymbol{u}_\mathrm{m}(\boldsymbol{x}) \approx \boldsymbol{u}^h_\mathrm{m}(\boldsymbol{x}) = \sum_{i=1}^{n} N_i(\boldsymbol{x})\,\boldsymbol{u}_i = \boldsymbol{N}_\mathrm{u}\boldsymbol{d}, \tag{2}$$

where $N_i(\boldsymbol{x})$ and $\boldsymbol{u}_i$ are the standard Lagrange shape function and displacement vectors defined at node i, respectively, the number of nodes in an element is n, the matrix $\boldsymbol{N}_\mathrm{u}$ contains elemental shape functions, and $\boldsymbol{d}$ is the nodal displacement vector. Stiffness matrix

$$\boldsymbol{K}^e_\mathrm{m} = \int_{\Omega^e_\mathrm{m}} \boldsymbol{B}^\mathrm{T}_\mathrm{u}\boldsymbol{D}_\mathrm{m}\boldsymbol{B}_\mathrm{u}\,\mathrm{d}\Omega_\mathrm{m} \tag{3}$$

and external force vector

$$\boldsymbol{f}^e_\mathrm{ext} = \int_{\Gamma^e_\mathrm{t}} \boldsymbol{N}^\mathrm{T}_u\bar{\boldsymbol{t}}\,\mathrm{d}\Gamma, \tag{4}$$

with $\boldsymbol{D}_\mathrm{m}$ the matrix of elastic constants and $\boldsymbol{B}_\mathrm{u}$ the matrix of shape function derivatives, are obtained following standard procedures applied to the first and last terms in (1).

2.2.2. Solid fiber model

A reference computational model is developed by meshing the exact geometry of the fiber in Ω_f with solid-type elements and by using a conformal discretization at the matrix-fiber interface. Although highly accurate, this approach requires the construction of

a conformal discretization, a tedious operation for many practical problems. Here, both matrix and fiber regions are discretized using conventional non-structured linear tetrahedral elements as shown in Fig. 1a for an inclined cylindrical fiber.

Using the counterpart of (2) for the fiber displacement field, the stiffness contribution related to the second term in (1) is

$$\boldsymbol{K}_{\mathrm{f}}^{e} = \int_{\Omega_{\mathrm{f}}^{e}} \boldsymbol{B}_{\mathrm{u}}^{\mathrm{T}} \boldsymbol{D}_{\mathrm{f}} \boldsymbol{B}_{\mathrm{u}} \, \mathrm{d}\Omega_{\mathrm{f}}, \tag{5}$$

where $\boldsymbol{D}_{\mathrm{f}}$ is the matrix of elastic constants of the fiber material.

To discretize the interface gap vector $\boldsymbol{w}$, zero-thickness conformal interface elements are included between matrix and fiber. This requires finding all matrix elements sharing at least one node with fiber elements (shaded in red in Fig. 1a); shared nodes are then duplicated and zero-thickness interface elements are embedded between matrix and fiber as depicted in Fig. 1b. The discretized interface gap vector,

$$\boldsymbol{w}^{h} = \boldsymbol{R}\boldsymbol{N}_{\mathrm{int}} \, \boldsymbol{d}_{\mathrm{int}}, \tag{6}$$

is expressed in a coordinate system local to the interface. Without loss of generality and by making reference to the node numbering in Fig. 1b, this is achieved by defining the rotation matrix $\boldsymbol{R}$ from the global to the local coordinate system, the interface shape functions matrix

$$\boldsymbol{N}_{\mathrm{int}} = \left[\boldsymbol{N}_{\mathrm{int}}^{\mathrm{f}} \mid \boldsymbol{N}_{\mathrm{int}}^{\mathrm{m}} \right] = \left[N_1 \boldsymbol{I} \quad N_2 \boldsymbol{I} \quad N_3 \boldsymbol{I} \mid -N_4 \boldsymbol{I} \quad -N_5 \boldsymbol{I} \quad -N_6 \boldsymbol{I} \right] \tag{7}$$

expressed in terms of isoparametric coordinates for the zero-thickness interface element, and the interface nodal displacement vector

$$\boldsymbol{d}_{\mathrm{int}} = \left[\boldsymbol{u}_{\mathrm{f1}} \quad \boldsymbol{u}_{\mathrm{f2}} \quad \boldsymbol{u}_{\mathrm{f3}} \mid \boldsymbol{u}_{\mathrm{m4}} \quad \boldsymbol{u}_{\mathrm{m5}} \quad \boldsymbol{u}_{\mathrm{m6}} \right]^{\mathrm{T}}, \tag{8}$$

where $\boldsymbol{I}$ is the identity matrix of size three, and $\boldsymbol{u}_{\mathrm{f}i\,(i=1,2,3)}$ and $\boldsymbol{u}_{\mathrm{m}i\,(i=4,5,6)}$ indicate the displacement vectors for fiber and matrix, respectively, in the global coordinate system.

Following standard procedures, the interface stiffness contribution

$$\boldsymbol{K}_{\mathrm{int}}^{e} = \int_{\Gamma_{\mathrm{int}}} \boldsymbol{N}_{\mathrm{int}}^{\mathrm{T}} \boldsymbol{R}^{\mathrm{T}} \boldsymbol{D}_{\mathrm{b}} \boldsymbol{R} \boldsymbol{N}_{\mathrm{int}} \, \mathrm{d}\Gamma_{\mathrm{int}} \tag{9}$$

is obtained on substituting (6) into the third term in (1) and with the interface constitutive matrix $\boldsymbol{D}_{\mathrm{b}} = \frac{\partial \boldsymbol{t}_{\mathrm{c}}}{\partial \boldsymbol{w}} = \mathrm{diag}(K_{\mathrm{bt}}, K_{\mathrm{bn1}}, K_{\mathrm{bn2}})$ for a linear elastic interface. The constants K_{bn1} and K_{bn2} represent the stiffnesses of the interface in the direction normal to the interface surface and perpendicular to it and to the fiber axis, respectively, and K_{bt} represents the stiffness of the interface in the direction tangential to the fiber axis. In this work, we only allow fiber slip in the direction tangential to the fiber axis by constraining the normal displacement gaps by means of penalty augmentation of the interface stiffnesses K_{bn1} and K_{bn2}. Additionally, interface elements are not introduced at the fiber endpoints where we assume no adhesion between fiber and matrix.

Expansion of the interface stiffness contribution (9), considering that the interface gap vector (6) is a function of both matrix and fiber displacements, results in

$$\begin{aligned} \boldsymbol{K}_{\mathrm{int}}^{e} &= \begin{bmatrix} \boldsymbol{K}_{\mathrm{int}}^{\mathrm{mm}} & \boldsymbol{K}_{\mathrm{int}}^{\mathrm{mf}} \\ \boldsymbol{K}_{\mathrm{int}}^{\mathrm{fm}} & \boldsymbol{K}_{\mathrm{int}}^{\mathrm{ff}} \end{bmatrix} \\ &= \begin{bmatrix} \int_{\Gamma_{\mathrm{int}}} \boldsymbol{N}_{\mathrm{int}}^{\mathrm{m}\,\mathrm{T}} \boldsymbol{R}^{\mathrm{T}} \boldsymbol{D}_{\mathrm{b}} \boldsymbol{R} \boldsymbol{N}_{\mathrm{int}}^{\mathrm{m}} \, \mathrm{d}\Gamma_{\mathrm{int}} & \int_{\Gamma_{\mathrm{int}}} \boldsymbol{N}_{\mathrm{int}}^{\mathrm{m}\,\mathrm{T}} \boldsymbol{R}^{\mathrm{T}} \boldsymbol{D}_{\mathrm{b}} \boldsymbol{R} \boldsymbol{N}_{\mathrm{int}}^{\mathrm{f}} \, \mathrm{d}\Gamma_{\mathrm{int}} \\ \int_{\Gamma_{\mathrm{int}}} \boldsymbol{N}_{\mathrm{int}}^{\mathrm{f}\,\mathrm{T}} \boldsymbol{R}^{\mathrm{T}} \boldsymbol{D}_{\mathrm{b}} \boldsymbol{R} \boldsymbol{N}_{\mathrm{int}}^{\mathrm{m}} \, \mathrm{d}\Gamma_{\mathrm{int}} & \int_{\Gamma_{\mathrm{int}}} \boldsymbol{N}_{\mathrm{int}}^{\mathrm{f}\,\mathrm{T}} \boldsymbol{R}^{\mathrm{T}} \boldsymbol{D}_{\mathrm{b}} \boldsymbol{R} \boldsymbol{N}_{\mathrm{int}}^{\mathrm{f}} \, \mathrm{d}\Gamma_{\mathrm{int}} \end{bmatrix}. \end{aligned} \tag{10}$$

2.2.3. Dimensionally-reduced fiber model

When modeling high aspect ratio fibers, the conforming finite element model described in the previous section can be replaced by a mesh-independent dimensionally-reduced model with a drastic reduction of the computational cost.

In the proposed model, inspired by embedded reinforcement techniques (Balakrishnan and Murray, 1986; Elwi and Hrudey, 1989; Barzegar and Maddipudi, 1997), fibers are idealized as one-dimensional objects that respond to axial deformation only. This is a reasonable assumption when dealing with high aspect ratio fibers. A fiber discretization independent from the matrix discretization and consisting of linear one-dimensional Lagrange elements is used to represent embedded fibers. Fig. 2 shows the case of a single embedded fiber although there are no limitations on the number of fibers that can cross a matrix element. Worth noticing is the independence of the two discretizations: fiber nodes do not coincide with intersection points between fiber axis and element faces. While any structured or unstructured fiber discretization can be used, in the numerical simulations in this paper fiber nodes are uniformly distributed for convenience.

To simplify the generation of the stiffness matrix for elements that are intersected by one-dimensional fibers, stiffness matrix (3), with the integration performed over the total volume Ω^{e} of the element, is used for the matrix contribution. This however requires the use of an effective Young's modulus for the fibers to cancel out the already considered matrix contribution in the fiber region. The contribution of the kth fiber element (with endpoints a and b for the red fiber element in Fig. 2) is identical to the stiffness matrix of a one-dimensional standard truss element in three-dimensional space and is written as

$$\boldsymbol{K}_{\mathrm{f}}^{k} = \frac{(E_{\mathrm{f}}^{k} - E_{\mathrm{m}}) \, A^{k}}{L^{k}} \begin{bmatrix} \boldsymbol{T}^{k} & -\boldsymbol{T}^{k} \\ -\boldsymbol{T}^{k} & \boldsymbol{T}^{k} \end{bmatrix}, \tag{11}$$

where E_{m} and E_{f}^{k} are the matrix and fiber Young's moduli, respectively, A^{k} is the cross sectional area ($A^{k} = \pi d_{\mathrm{f}}^{2}/4$ with d_{f} the fiber diameter), and L^{k} is the fiber element length. The fiber orientation matrix

$$\boldsymbol{T}^{k} = \begin{bmatrix} e_x^k e_x^k & e_x^k e_y^k & e_x^k e_z^k \\ e_x^k e_y^k & e_y^k e_y^k & e_y^k e_z^k \\ e_x^k e_z^k & e_y^k e_z^k & e_z^k e_z^k \end{bmatrix} \tag{12}$$

with

$$e_x^k = \frac{x_b^k - x_a^k}{L^k} \quad , \quad e_y^k = \frac{y_b^k - y_a^k}{L^k} \quad , \quad e_z^k = \frac{z_b^k - z_a^k}{L^k}, \tag{13}$$

where (x_a, y_a, z_a) and (x_b, y_b, z_b) indicate the coordinates of the fiber element ends (e.g., nodes a and b for the red fiber element in Fig. 2).

Consequently, the matrix-fiber interface is reduced to an equivalent line object, with interface gap vector (6) and stiffness matrix contribution (9) evaluated along it. The interface gap vector (6) is defined with

$$\boldsymbol{N}_{\mathrm{int}} = \left[\boldsymbol{N}_{\mathrm{int}}^{\mathrm{f}} \mid \boldsymbol{N}_{\mathrm{int}}^{\mathrm{m}} \right] = \left[N_a^{\mathrm{f}} \boldsymbol{I} \quad N_b^{\mathrm{f}} \boldsymbol{I} \mid -N_1^{\mathrm{m}} \boldsymbol{I} \quad \cdots \quad -N_n^{\mathrm{m}} \boldsymbol{I} \right] \tag{14}$$

and

$$\boldsymbol{d}_{\mathrm{int}} = \left[\boldsymbol{u}_a^{\mathrm{f}} \quad \boldsymbol{u}_b^{\mathrm{f}} \mid \boldsymbol{u}_1^{\mathrm{m}} \quad \cdots \quad \boldsymbol{u}_n^{\mathrm{m}} \right]^{\mathrm{T}}, \tag{15}$$

where N_a^{f} and N_b^{f} are the one-dimensional Lagrange shape functions at nodes a and b defined in an isoparametric coordinate system local to the fiber, and the shape function N_i^{m} at node i of the parent matrix element is also defined in an isoparametric coordinate system.

In a small deformation setting, the interface gap vector is evaluated in the undeformed configuration at integration points within fiber elements (e.g., at a and b for the red fiber element in Fig. 2 since we consider a two-point Gauss–Lobatto quadrature scheme). This implies that once the local coordinates of an integration point along a fiber element are defined, they are expressed into the global coordinate system and used to identify its parent matrix element by means of an octree structure (Duflot, 2006, Section 9.1) that is constructed prior to the analysis.

The fiber shape function in (14) are directly evaluated at the integration point in an isoparametric coordinate system local to the fiber. The shape function of the matrix element are also evaluated at the same point now expressed in the isoparametric coordinate system related to the matrix element and obtained through an inverse mapping procedure starting from its position in the global coordinate system. Matrix and fiber elements are connected through so-called bond elements that are defined with reference to the two fiber element nodes and the nodes of the matrix element in which the fiber element nodes are located (the discretization is therefore conforming on the side of the fiber and not conforming on the side of the matrix, and a fiber element can have nodes in two distinct matrix elements).

The interface contribution (9) related to the kth fiber element becomes

$$\boldsymbol{K}^k_{\text{int}} = C^k_{\text{f}} \int_{L^k} \boldsymbol{N}^{\text{T}}_{\text{int}} \boldsymbol{R}^{\text{T}} \boldsymbol{D}_{\text{b}} \boldsymbol{R} \boldsymbol{N}_{\text{int}} \, \text{d}s, \tag{16}$$

with $C^k_{\text{f}} = \pi d_{\text{f}}$ the circumference of the fiber, L^k the length of fiber-matrix bond element, and s the local coordinate along the bond element. Thus, for a system with n_{f} fibers each subdivided into n_{s} line elements, as shown in Fig. 2, the total number of fiber and interface element contributions is equal to $2 \times n_{\text{f}} \times n_{\text{s}}$. Similar to (10), the interface contribution is shared between matrix and fiber degrees of freedom in the assembly of the corresponding stiffness matrix.

2.2.4. Global system of equations

The $n_{\text{f}} \times n_{\text{s}}$ fiber element contributions and $n_{\text{f}} \times n_{\text{s}}$ matrix-fiber interface element contributions to the global stiffness matrix are assembled separately from those of the matrix elements. Irrespective of the fiber discretization scheme, the general form of global system of equations is

$$\begin{bmatrix} \boldsymbol{K}_{\text{mm}} & \boldsymbol{K}_{\text{mf}_1} & \boldsymbol{K}_{\text{mf}_2} & \dots & \boldsymbol{K}_{\text{mf}_{n_{\text{f}}}} \\ \boldsymbol{K}_{\text{f}_1\text{m}} & \boldsymbol{K}_{\text{f}_1\text{f}_1} & \boldsymbol{0} & \dots & \boldsymbol{0} \\ \boldsymbol{K}_{\text{f}_2\text{m}} & \boldsymbol{0} & \boldsymbol{K}_{\text{f}_2\text{f}_2} & \dots & \boldsymbol{0} \\ \vdots & \vdots & \vdots & \ddots & \vdots \\ \boldsymbol{K}_{\text{f}_{n_{\text{f}}}\text{m}} & \boldsymbol{0} & \boldsymbol{0} & \dots & \boldsymbol{K}_{\text{f}_{n_{\text{f}}}\text{f}_{n_{\text{f}}}} \end{bmatrix} \begin{bmatrix} \boldsymbol{m} \\ \boldsymbol{f}_1 \\ \boldsymbol{f}_2 \\ \vdots \\ \boldsymbol{f}_{n_{\text{f}}} \end{bmatrix} = \begin{bmatrix} \boldsymbol{F}_{\text{m}} \\ \boldsymbol{0} \\ \boldsymbol{0} \\ \vdots \\ \boldsymbol{0} \end{bmatrix}, \tag{17}$$

where $\boldsymbol{m}$ and $\boldsymbol{f}_i$ $(i = 1, \dots, n_{\text{f}})$ are vectors containing matrix and individual fiber displacements, respectively. The submatrices in the global stiffness matrix in (17) are assembled by applying standard procedures to elemental stiffness contributions of matrix, fiber and matrix-fiber interface. In this framework, matrix and fiber stiffnesses lead to block diagonal terms while, as shown in (10), interface contributions ensuring the coupling between matrix and fibers lead to both block diagonal and block off-diagonal terms.

Throughout this study, linear elastic behavior is assumed for the constitutive models of matrix, fiber, and matrix-fiber interface.

3. Validity of the dimensionally-reduced approach

The influence of the one-dimensional reduction of the fiber geometry on the mechanical response of a fiber-reinforced composite is studied. The geometrical reduction is performed over the fiber diameter d_{f}, with fixed fiber length l_{f}. The validation of the dimensionally-reduced fiber model is performed against the solid fiber model described in Section 2.2.2 assuming the ratio between fiber diameter and domain size L as the characterizing parameter. To reduce the complexity of the discretization procedures due to the generation of a conforming mesh, only one fiber is considered in the configuration shown in Fig. 1a for the reference model. Unless stated otherwise, in all the simulations in this paper we have assumed that matrix Young's modulus E_{m} and Poisson's ratio ν_{m} are equal to 100 MPa and 0.4, respectively, and that in the solid fiber model, matrix and fiber have the same Poisson's ratio. Further, the effective mechanical properties of the composite are estimated through the procedure described in Appendix A.

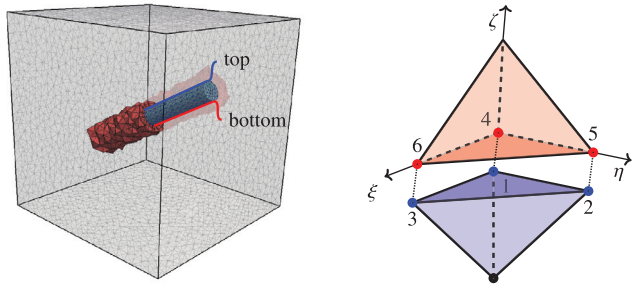

Fig. 1. (a) Reference conformal finite element model with a cylindrical fiber that is discretized using tetrahedral finite elements. (b) Zero-thickness conformal interface elements are placed between fiber (blue region) and surrounding matrix (red region) to allow fiber slip. It is assumed that no adhesion exists between the endpoints of the fiber and the matrix. (For interpretation of the references to colour in this figure legend, the reader is referred to the web version of this article.)

3.1. Perfect bond: Effective mechanical properties

We now determine the range of fiber diameters over which the predictions of the dimensionally-reduced fiber model are valid. To this end, we compute the values of the effective longitudinal Young's modulus E^{c}_x of a composite with one fiber aligned with the x-axis ($\theta_z = 0^\circ$ in Fig. 3) and compare them to the corresponding values obtained with the solid fiber model. It should be mentioned that this orientation is chosen among all orientations in the xy plane because it yields the largest increase in E^{c}_x. Computations are done with two different fiber lengths ($l_{\text{f}} = 0.4L$ and $l_{\text{f}} = 0.8L$). A large value of the interface tangential stiffness K_{bt} is used to mimic a perfectly bonded interface (hereafter referred to as perfect interface). Fig. 4 shows the effective composite Young's modulus E^{c}_x for various values of the fiber Young's modulus E_{f}, both normalized by the matrix Young's modulus E_{m}. By reducing the ratio d_{f}/L, the responses of the numerical models converge to the same value. For $d_{\text{f}}/L < 0.01$ a very good agreement between them holds, and a one-dimensional representation of the fiber can be justified.

3.2. Imperfect bond: Matrix-fiber slip

Next, we study how the slip profiles between matrix and fiber compare for the reduced model and the solid fiber model when a linear elastic traction separation law is employed. While the dimensionally-reduced fiber model obviously generates one slip profile, an infinite number of slip profiles can be sampled with the solid-fiber model. To obtain a visually meaningful representation of the results, we have considered a very weak interface ($K_{\text{bt}} = 500\ \text{N/mm}^3$), hereafter referred to as imperfect interface. The simulation box is deformed in the horizontal direction through the imposition of a periodic strain ($\varepsilon_{xx} = 0.1$) as discussed in Appendix A. This computational setup eliminates the influence of the domain size L from the results. Fig. 5a (5b) shows the resulting normalized fiber slip profiles for a fiber aligned with the loading direction ($\theta_z = 0^\circ$) and fiber diameter $d_{\text{f}} = 0.03L$ ($0.005L$). With reference to the solid fiber model, in this special case the points surrounding the fiber at the same horizontal coordinate experience the same displacement with respect to the corresponding fiber points. A unique slip profile is therefore generated which is found to be in a remarkably good agreement with the slip profile generated by the dimensionally-reduced fiber model. In contrast, as shown in Figs. 5c and d, an inclined fiber ($\theta_z \approx 28.6^\circ (= 0.5\,\text{rad})$)

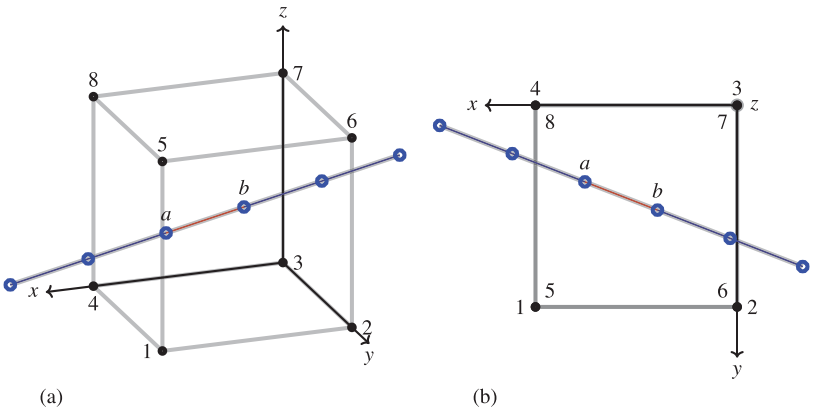

Fig. 2. A dimensionally-reduced fiber intersects a solid matrix element: (a) three-dimensional view, (b) top view. The fiber can be placed within the solid element region and can be discretized independently from it. Discretized fiber elements are shown in blue, separated by nodes. The figure shows also a fiber element, in red, between nodes a and b. (For interpretation of the references to colour in this figure legend, the reader is referred to the web version of this article.)

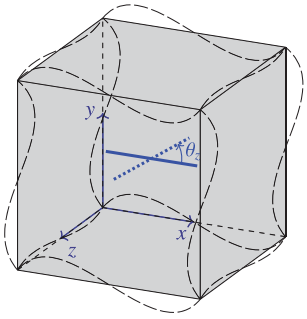

Fig. 3. An $L \times L \times L$ ($L = 1$ mm) periodic simulation box with a fiber of length l_f in the middle aligned along the x axis. In the fiber orientation study (Section 4.1), the fiber can rotate around the z axis by an angle θ_z in the xy plane.

does not slide uniformly with respect to the surrounding material. The gray shaded region represents all the fiber slip profiles sampled over the lateral surface in directions parallel to the fiber axis. These displacement slip profiles cannot be predicted by the reduced model where, instead, a single slip profile is predicted (dashed lines), which is however in good agreement with the average slip profile of the solid fiber model.

As shown in Figs. 5c and d, the width of the shaded region decreases by reducing the fiber diameter indicating that the difference between the upper and lower interface displacement gap vectors becomes smaller. This means that the results obtained with the solid fiber model converge to those of the dimensionally-reduced fiber model as the fiber diameter decreases. To generalize the relation between fiber diameter and interfacial displacement gaps for inclined fibers, the normalized area A_e of the shaded region, referred to as normalized gap area, is plotted against the normalized fiber diameter in Fig. 6. Results are shown in Fig. 6a for different values of the fiber Young's modulus E_f and fiber length l_f. Irrespective of fiber length and material properties, the normalized gap area decreases with decreasing fiber diameter, and its value is obviously a function of fiber orientation, decreasing with decreasing fiber orientation angle as illustrated in Fig. 6b.

4. Fiber neutrality

According to previous studies on planar reinforcements, perfectly bonded rigid inclusions become mechanically neutral under specific circumstances—mechanically neutral inclusions do not influence the mechanical response of the composite. Wang et al. (1985) have derived the analytical solution for a zero-thickness RLI subjected to an inclined loading at infinity; for a given in-plane problem (plane stress/plane strain), the angle between the loading direction and the RLI at which the inclusion does not influence the stress field depends only on the Poisson's ratio of the matrix material. A similar property has not yet been reported in fiber-reinforced composites despite various studies on the role of fiber orientation in their homogenized mechanical properties (Tian et al., 2016; 2014; Kang and Gao, 2002). Motivated by these observations, we perform a study on orientation effects and stress neutrality properties for linear elastic thin (high aspect ratio) fibers with imperfect matrix-fiber interface.

4.1. Neutrality in the dimensionally-reduced model

Neutral orientations are determined for effective Young's and shear moduli and Poisson's ratios. For the sake of illustration, specimens with fiber volume fraction $v_f = 1.0\%$ (1300 aligned fibers) are considered. Length and diameter of the fibers, discretized with the dimensionally-reduced model, are set to $0.2L$ and $0.007L$, respectively. The results have been obtained with the numerical homogenization procedure described in Appendix A. Numerical effective properties of the homogenized composite are reported in Fig. 7a for fiber orientations θ_z ranging from 0° to 90°. In the simulations, the ratio E_f/E_m is set to 100 and an imperfect interface between fiber and matrix is assumed. Although we present results for this specific set of material properties, their validity for other parameter sets, also including the case of a rigid interface, was confirmed with simulations whose results are not reported here. A comparison with analytical micromechanical estimates is provided in Section 5.

As expected, the highest effective Young's modulus is obtained when fibers are aligned with the loading direction. Contrary to the general understanding that fibers always increase the stiffness of a fiber-reinforced composite, corroborated also by results obtained with two-step mean-field homogenization procedures (see, e.g., Pierard et al. (2004, Fig. 3) and Tian et al. (2016, [Figs. 7–10]), the minimum composite stiffness corresponds to a state of fiber neutrality. It is additionally implied from Fig. 7a that fibers perpendicular to the loading direction ($\theta_z = 90°$) can, in general, increase the effective Young's modulus of the composite.

Fiber orientations corresponding to a neutral situation (i.e., neutral orientations θ_n at which fibers have no influence on the Young's modulus of the composite) are function of the Poisson's ratio ν_m of the matrix material only and are reported in Fig. 7b (blue-filled circles). In the same figure we report values for plane states corresponding to the cases of unperturbed stress fields around a zero-thickness perfectly-bonded rigid planar inclusion according to the analytical solution by Wang et al. (1985). It is inter-

esting to notice that dimensionally-reduced fibers are mechanically neutral at the neutral orientations valid for RLIs in a plane stress state.

As shown in Fig. 8, neutrality is observed in terms of the effective shear modulus G^c_{xy} of the composite as well. In this case, neutral orientations are 0° and 90°. A similar stress neutrality has been reported in RLIs under uniform shear loading by Noselli et al. (2010) using photoelasticity in a two-dimensional experimental study. Finally, various cases of neutrality in terms of the effective anisotropic Poisson's ratios can be identified in Fig. 9.

These results confirm that linear elastic thin fibers share the neutrality feature of zero-thickness RLIs (i.e., the neutrality angle depends only on the matrix Poisson's ratio). As already mentioned, neutrality holds irrespective of fiber-matrix interface parameter. This is at variance with previously known cases of neutrality of arbitrary shaped inhomogeneities (Ru, 1998; Benveniste and Miloh, 1999) in which neutrality is achieved by designing non-ideal or imperfect interfaces between inclusion and matrix.

4.1.1. Fiber compression under tensile loading

At neutral orientations θ_n shown in Fig. 7b, a fiber does not experience deformation. This implies a sign shift in the fiber strain and slip. Fig. 10 shows the slip and strain profiles in the fiber of the one-fiber composite depicted in Fig. 3 under tensile loading along the x-axis at various orientations (neutral angle $\theta_n \approx 55°$). Results are shown for the case of a nearly incompressible matrix with $\nu_m = 0.49$; the values of all other properties are taken from the example in the previous section. A similar set of results can be obtained for other matrix Poisson's ratios.

A shift in sign when θ_z exceeds the neutrality angle θ_n can be detected in both fiber slips and strain profiles. Tensile strains occur in fibers with orientations below θ_n while for orientations exceeding θ_n the sign reverses and compressive strains along the fiber axis are generated. This behavior could trigger composite failure in the form of fiber micro-buckling (Budiansky and Fleck, 1993), even with externally applied tensile forces.

4.2. Neutrality and fiber diameter in the solid fiber model with perfect interface

In the previous section we have shown, using the dimensionally-reduced fiber model, that linear elastic thin fibers with imperfect matrix-fiber interface are neutral under specific circumstances. We now investigate how the fiber diameter influences this property considering a perfectly bonded solid fiber. The case of an imperfect matrix-fiber interface is discussed in the next section. The results are obtained using the simulation box in Fig. 3 with one perfectly bonded fiber (length $l_f = 0.8L$) that is discretized using the solid and the dimensionally-reduced fiber models.

To investigate the relation between fiber diameter and the occurrence of fiber neutrality, the fiber is oriented along the neutral orientation that was determined for the dimensionally-reduced fiber model ($\theta_z = \theta_n \approx 57°$ from Fig. 7b, for a matrix with Poisson's ratio $\nu_m = 0.4$). The normalized effective Young's modulus E^c_x is reported in Fig. 11 at different fiber diameters and stiffnesses. For the sake of comparison with the longitudinal Young's modulus, which gives the maximum achievable effective stiffness, solid fiber model results for the case with $\theta_z = 0°$ are also included in the plots.

As shown in Fig. 11, the dimensionally-reduced model predicts neutrality at all fiber diameters when $\theta_z \approx 57°$ (black curves in Fig. 11). Since the fiber is described as a line object, this is attributed to the fact that the diameter is not geometrically incorporated in an explicit manner but is considered as a parameter in the fiber and interface contributions to the stiffness matrix. However, when the exact geometry of the fiber is taken into account using the solid fiber model (blue curves in Fig. 11), neutrality holds only for relatively small fiber diameters ($d_f/L < 0.01$). For $d_f/L > 0.01$ the increase of the effective Young's modulus is modest and is not significantly influenced by the fiber stiffness unlike the effective longitudinal Young's modulus (red curves).

Analogous observations hold for the effective shear modulus G^c_{xy}. Fig. 12 shows a comparison of the two fiber models at $\theta_z = 0°$ (according to Fig. 8, neutrality in terms of G^c_{xy} occurs at $\theta_z = 0°$). Results are now accompanied by the solid fiber model predictions for a fiber orientation ($\theta_z = 45°$) that yields the maximum effective shear stiffness.

These observations are somehow in agreement with previous numerical studies of fiber orientation in short fiber-reinforced metal matrix composites (Kang and Gao, 2002; Tian et al., 2016). In these studies a modest increase of the effective Young's and shear moduli was found for fibers inclined at $\theta_z = 60°$ and $\theta_z = 0°$ in short carbon fiber composites (fiber with aspect ratio 15, $d_f \approx 0.03L$). In contrast, in the results shown in Figs. 11 and 12, neutrality of fibers is expected at smaller diameters, and the effective stiffness of the composite will not change compared to the matrix stiffness computed at the orientations shown in Fig. 7b.

4.3. Neutrality and imperfect interface

Neutrality was already discussed in Section 4.1 under imperfect interface conditions with the analysis restricted to the single-interface assumption of the dimensionally-reduced fiber model. In this section, we discuss how neutrality can change considering the actual interface in a three-dimensional composite with a solid fiber and a two-dimensional planar composite with a thin inclusion.

4.3.1. Solid fibers in a three-dimensional composite

An imperfect interface leads to partial load transfer, with displacement jumps occurring between fiber and matrix. According to the non-uniqueness of the slip profile for an inclined fiber as discussed in Section 3.2, displacement differences between fiber edges (e.g., the top and bottom edges shown in Fig. 5c and d) can occur. For relatively small fiber diameters, however, displacement differences between edges become small and the slip profiles can be approximated by a unique curve. Here we further assess this approximation and the significance of the different slip profiles by emphasizing their effect on the development of stress neutrality.

Similar to Section 4.2, a composite with one fiber oriented at the neutral orientation ($\theta_z = \theta_n \approx 57°$ from Fig. 7b, $\nu_m = 0.4$) is discretized using the solid fiber model. Values of Young's modulus E^c_x are plotted as a function of fiber diameter in Fig. 13 for both perfect and imperfect interfaces. For the sake of comparison, the Young's moduli obtained with the solid fiber model with $\theta_z = 0°$ (black lines) are also included in the plot for both interface conditions. Compared to the perfect interface case (solid lines), an imperfect interface (dashed lines) leads in general to lower values of the effective longitudinal Young's modulus E^c_x. More specifically, when the angle $\theta_z \approx 57°$, the reduction is only pronounced at relatively large fiber diameters; at small fiber diameters ($d_f/L < 0.01$) the longitudinal Young's modulus of the composite converges to the value of the Young's modulus of the matrix and, with a perfect or imperfect interface, a neutral state is predicted. When $\theta_z = 0°$ a reduced stiffness is detectable even at small fiber diameters (see inset in Fig. 13).

To summarize, irrespective of the interface type, a fiber with a small diameter compared to the characteristic dimension of the domain is not strained when inclined at $\theta_z = \theta_n \approx 57°$ (neutral orientation for $\nu_m = 0.4$) and has therefore a null effect on the stiffness of the composite.

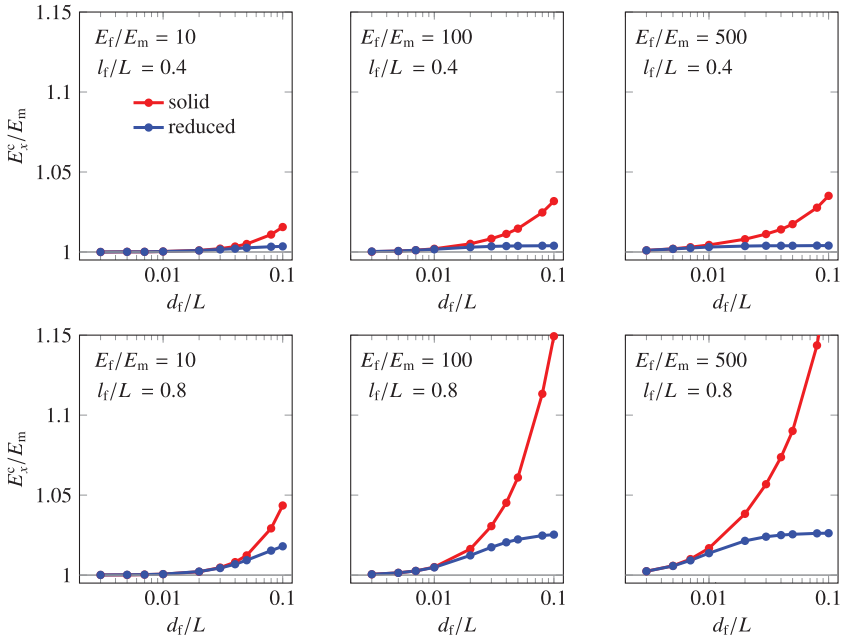

Fig. 4. Normalized effective composite Young's modulus as a function of fiber diameter for a fiber with aspect ratio between 4 and 266. Predictions of both models agree for small fiber diameters relative to the domain size.

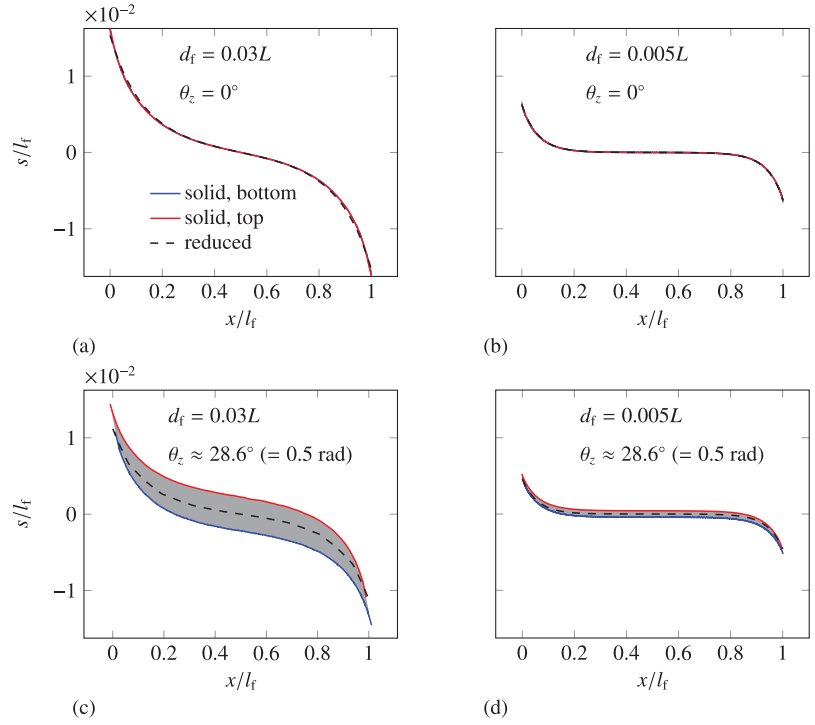

Fig. 5. Normalized fiber slip s for a single embedded fiber with imperfect interface with $E_f/E_m = 10$ and $l_f = 0.8L$. (a,b) A unique slip profile can be identified for a fiber aligned with the loading direction. (c,d) The slip profile is not unique for an inclined fiber. The dimensionally-reduced model produces a unique slip profile that agrees with the average slip of the solid fiber model (dashed line). Refer to Fig. 1a for the nomenclature used for the solid fiber model.

4.3.2. Dimensionally-reduced inclusion in a two-dimensional composite

The two-dimensional conformal model in Fig. 14, obtained as a limit case of the previously discussed solid fiber model, can adequately model certain types of two-dimensional composites (Sheng et al., 2004; Hall et al., 2008). The model is employed to investigate the occurrence of neutral states (reported in Wang et al. (1985) for perfectly-bonded two-dimensional planar inclusions) under imperfect interface conditions. In this computational setting, two interface surfaces can be identified when the inclusion is not perfectly bonded to the matrix: one at each side of the inclusion and physically disconnected from each other. Depending on the out of plane shape of the inclusion, different assumptions can be made regarding the continuity of the displacement field across it. For a situation with platelet inclusions, as in clay nanocomposites (Sheng et al., 2004), displacement jumps across the platelet adequately represent the expected kinematics even for platelets of small thickness. As soon as the inclusion out-of-plane dimen-

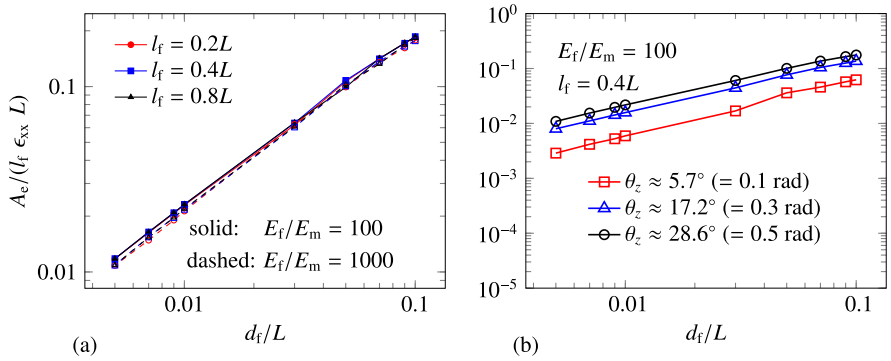

Fig. 6. Effect of fiber diameter on the normalized gap area for a fiber with aspect ratio between 2 and 160. (a) Normalized gap area for fibers with different properties and $\theta_z \approx 28.6°$ (= 0.5 rad). (b) Normalized gap area for different fiber rotations θ_z.

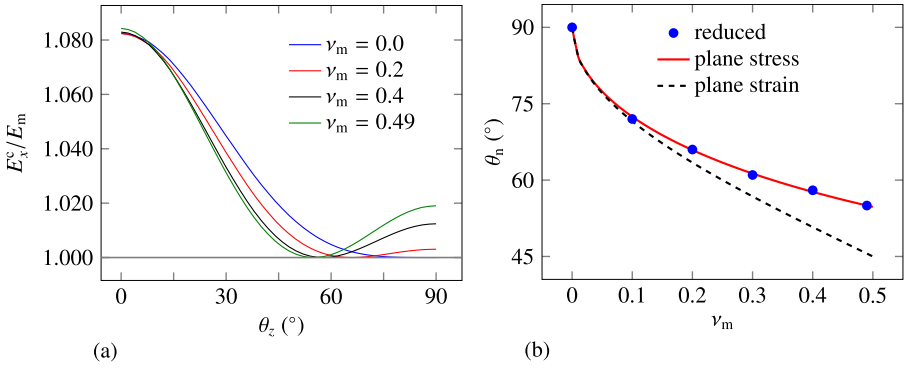

Fig. 7. (a) Normalized effective Young's modulus E_x^c calculated at various fiber orientations θ_z and matrix Poisson's ratios ν_m. (b) The neutral orientation θ_n is the orientation corresponding to fibers experiencing no deformation under the applied load. Results obtained with $E_f/E_m = 100$, $K_{bt} = 500$ N/mm^3, and $\upsilon_f = 1\%$ (1300 aligned fibers with $d_f = 0.007L$ and $l_f = 0.2L$). Plane stress and plane strain results are from Wang et al. (1985). (For interpretation of the references to colour in this figure legend, the reader is referred to the web version of this article.)

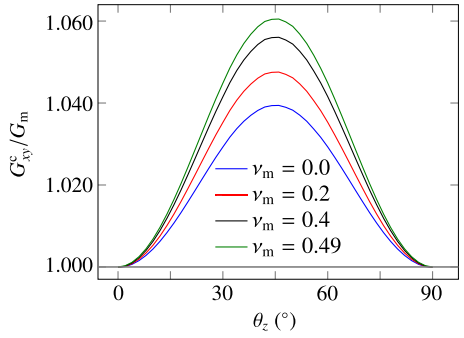

Fig. 8. Normalized effective shear modulus G_{xy} calculated at various fiber orientations θ_z and matrix Poisson's ratios ν_m. Results obtained with $E_f/E_m = 100$, $K_{bt} = 500$ N/mm^3, and $\upsilon_f = 1\%$ (1300 aligned fibers with $d_f = 0.007L$ and $l_f = 0.2L$).

sion decreases and the inclusion represents a fiber, as in fiber networks in ordinary paper sheets or buckypaper (Hall et al., 2008), the double-interface model is not representative anymore, and a traditional single-interface model of the type described in Section 2.2.3 is to be preferred.

In the double-interface model shown in Fig. 14, conceptually similar to the model by Pike et al. (2015), zero-thickness interface elements are placed at each side of the inclusion to allow the occurrence of relative displacements between inclusion and matrix on both sides of the inclusion. In this situation, upper and lower interfaces move relative to each other. To describe this kinematics, the interface shape function matrix (7) is rewritten as

$$\boldsymbol{N}_{\text{int}}^{\text{t/b}} = \begin{bmatrix} N_1^{\text{i}} & 0 & N_2^{\text{i}} & 0 & -N_1^{\text{t/b}} & 0 & -N_2^{\text{t/b}} & 0 \\ 0 & N_1^{\text{i}} & 0 & N_2^{\text{i}} & 0 & -N_1^{\text{t/b}} & 0 & -N_2^{\text{t/b}} \end{bmatrix}, \tag{18}$$

where N_1^{i} and N_2^{i} are one-dimensional Lagrange shape functions evaluated at the inclusion end points 1 and 2, respectively. Similarly, $N_1^{\text{t/b}}$ and $N_2^{\text{t/b}}$ are the matrix nodal shape functions evaluated at points 1 and 2, and superscripts t and b denote top and bottom interfaces, respectively. The simpler single-interface model, which does not account for a discontinuous matrix displacement field, can be recovered by constraining the top and bottom nodes to experience the same displacement ($\boldsymbol{u}^t = \boldsymbol{u}^b$).

Figs. 15a–c show the effective mechanical properties of the 1 mm × 1 mm periodic plate with a centered 0.5 mm long inclined inclusion as a function of the inclusion orientation θ_z. Mechanical properties are extracted using the procedure described in Appendix A. In the analyses we used two values of the interfacial tangential stiffness K_{bt} (500 N/mm^2 and 1000 N/mm^2), and we assumed a unit thickness for the plate in the out-of-plane dimension. The relatively low values shown in Fig. 15 are a consequence of the choice of the parameters and the modest mechanical effect of a single fiber.

Fig. 15a shows that in the double-interface model the angle θ_z that corresponds to the minimum effective Young's modulus of the composite (marked in the figure) is a function of the interfacial tangential stiffness K_{bt}: the value of the angle increases with increasing values of K_{bt} and tends to $\approx 50.7°$. For the single-interface model, the value of K_{bt} has no effect on the angle at which E_x^c is at a minimum: this angle is equal to $\approx 50.7°$ and corresponds to the neutral orientation previously discussed (in this specific case, $\theta_n \approx 50.7°$ for $\nu_m = 0.4$ under plane strain as shown in Fig. 7b). This means that in the range of validity of the dimensionally-reduced model, E_x^c will assume its minimum value, corresponding to a situation of fiber neutrality, at the same inclusion angle shown in Fig. 7b, irrespective of the value of the interfacial tangential stiffness K_{bt}.

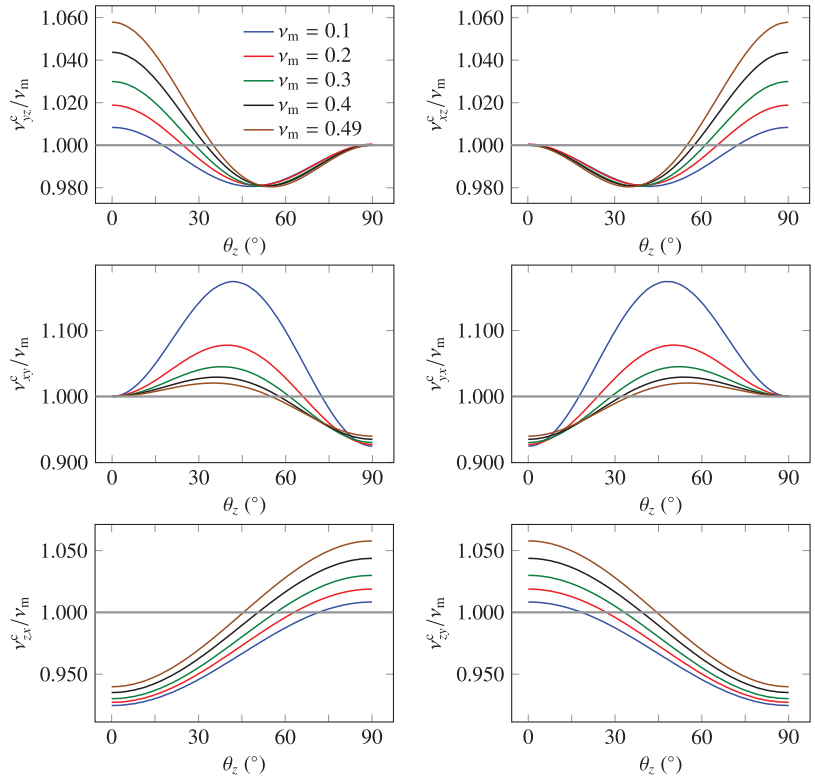

Fig. 9. Normalized effective Poisson's ratio calculated at various fiber orientations θ_z and matrix Poisson's ratios ν_m. Results obtained with $E_f/E_m = 100$, $K_{bt} = 500$ N/mm^3, and $\upsilon_f = 3\%$ (1300 aligned fibers with $d_f = 0.007L$ and $l_f = 0.2L$).

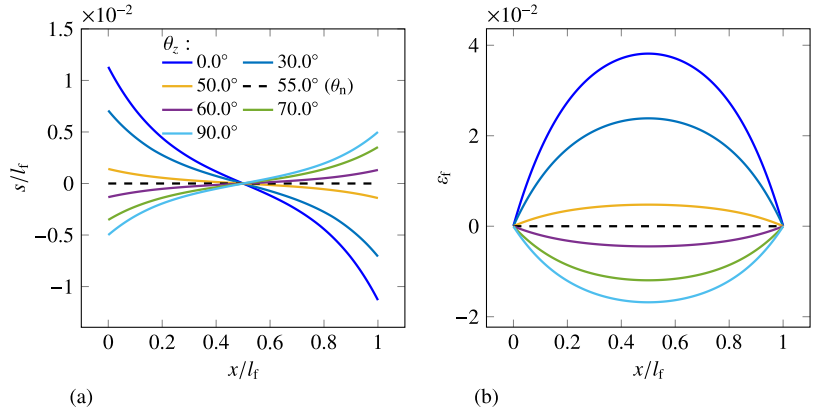

Fig. 10. A one-fiber composite with a nearly incompressible matrix material ($\nu_m = 0.49$) under the action of a horizontal external load. Fiber slip s (a) and fiber axial strains ε_f (b) are strongly influenced by the fiber orientation θ_z. Results obtained with $E_f/E_m = 100$, $K_{bt} = 500$ N/mm^3, $d_f = 0.007L$ and $l_f = 0.8L$.

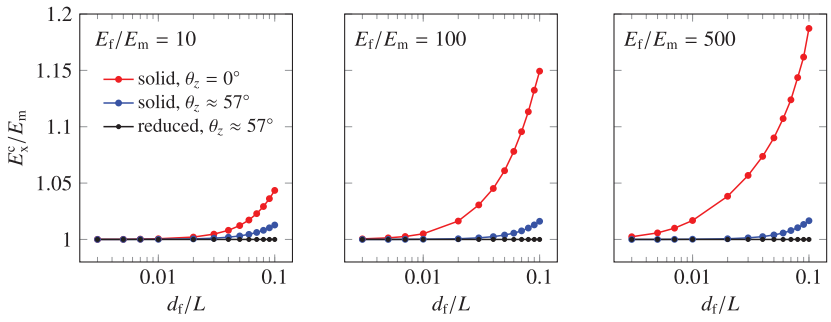

Fig. 11. Normalized effective Young's modulus of the one-fiber composite (with $l_f = 0.8L$) as a function of fiber diameter for solid and dimensionally-reduced models at neutral orientation (Fig. 7b: $\theta_z \approx 57°$ for $\nu_m = 0.4$) of the dimensionally-reduced model for a fiber with aspect ratio between 8 and 266. The longitudinal Young's modulus of a composite with a horizontal fiber ($\theta_z = 0°$) obtained with the solid fiber model (previously reported in Fig. 4, second row) is also included. (For interpretation of the references to colour in this figure legend, the reader is referred to the web version of this article.)

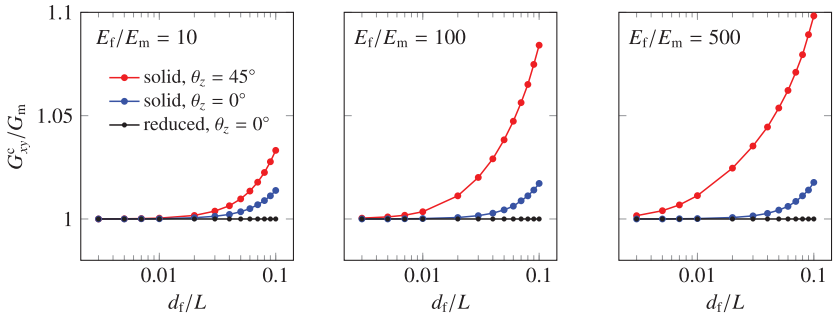

Fig. 12. Normalized effective shear modulus of the one-fiber composite (with $l_f = 0.8L$) as a function of fiber diameter for solid and dimensionally-reduced models at neutral orientation ($\theta_z = 0^\circ$ from Fig. 8, irrespective of ν_m) of the dimensionally-reduced model for a fiber with aspect ratio between 8 and 266. The maximum shear modulus obtained with the solid fiber model for a fiber inclined at $\theta_z = 45^\circ$ is also included.

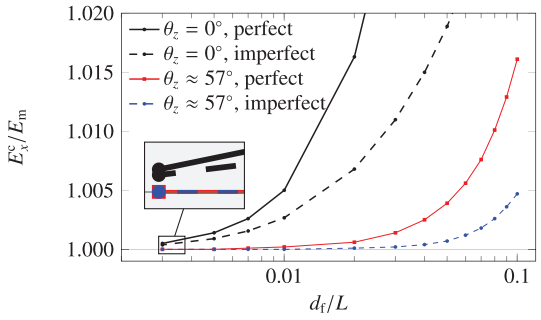

Fig. 13. Normalized Effective Young's modulus of a composite with one fiber oriented at the neutral orientation obtained with the dimensionally-reduced fiber model ($\theta_z \approx 57^\circ$ from Fig. 7b, $\nu_m = 0.4$) and discretized using the solid fiber model under perfect and imperfect interface conditions for a fiber with aspect ratio between 8 and 266. The longitudinal Young's moduli obtained with the solid fiber model (previously reported in Fig. 4, second row and second column) are also included. Both perfect and imperfect interface conditions are under a neutral state at small fiber diameters with $\theta_z = \theta_n \approx 57^\circ$. Results obtained with $E_f/E_m = 100$, $K_{bt} = 500$ N/mm^3 and $l_f = 0.8L$.

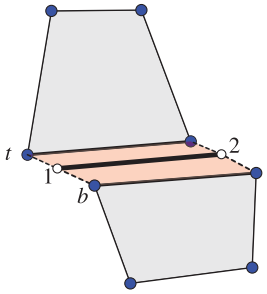

Fig. 14. Single conforming inclusion with elastic imperfect interface. Interface elements are placed at each side of the inclusion. For illustrative purposes, both normal and tangential displacement jumps are depicted.

In the single-interface model the angle corresponding to the minimum value of E^c_x indicates a situation of inclusion neutrality. In the double-interface model however we observe that i) the composite Young's modulus can be lower than that of the matrix for a wide range of inclusion angles (stiffness degradation), and ii) the amplitude of the range decreases with increasing K_{bt} values. Similar considerations can be drawn for the shear modulus in Fig. 15b although neutrality is only observed for the single-interface model at θ equal to 0° or 90°.

Under shear loading, relative movements between edges of the inclusion occur and, as shown in Fig. 15b, a similar reduction in the value of the effective shear modulus to a value lower than the matrix shear modulus is obtained with the double-interface model. Additionally, maximum shear modulus is achieved for $\theta_z = 45^\circ$, where predictions of single- and double-interface models are the same.

As for the Poisson's ratio in Fig. 15c, the double-interface model yields an increase of the composite effective Poisson's ratios ν_{xy} for all orientations compared to the single-interface model. For θ equal to 0° (90°), interfacial jumps (Fig. 15d) are absent and the effective Young's modulus and Poisson's ratio values are equal in both models.

Degradation is attributed to the crack-like features of the interface and is not expected when a single-interface model is used or under a perfect interface condition. In these situations, inclusion neutrality is expected at the previously defined neutral orientations. Moreover, the minimum angles for the double-interface model, indicated by red marks in Fig. 15a, and the degradation range are not only a function of the interface stiffness values, but are also affected by geometrical properties (e.g., fiber length, number of fibers, and their spatial arrangements).

5. Micromechanical analysis

Mesh-independent fiber models are a necessary tool for the modeling and simulation of composites with many fibers (Fig. 16). To this end, a detailed analysis, taking into account the fiber volume fraction as a variable, is presented in this concluding section. Estimates obtained from commonly used micro-mechanical models summarized in Appendix B are contrasted to results obtained with the dimensionally-reduced model. The occurrence of fiber neutrality is also investigated.

We consider equally-shaped fibers with length $l_f = 0.2L$ and diameter $d_f = 0.007L$ that are n times stiffer than the matrix material ($n = 10,\ 100,\ 500$). To compare the numerical results with those obtained with analytical micromechanical models, fibers and matrix are perfectly bonded. The simulation box is discretized using a uniform grid of $31 \times 31 \times 31$ trilinear hexahedral elements, and each fiber is subdivided into 20 equally-spaced segments. The mesh-convergence study in Fig. 17 confirms that the employed discretization is sufficiently accurate. As mentioned in the introduction, discontinuities in the stress field across a fiber are neglected in dimensionally-reduced models to favor numerical efficiency. The error introduced with this approximation is not negligible for high stiffness contrast values n and large fiber volume fractions υ_f. In such cases a slower convergence is observed (Fig. 17c). Distributions of homogeneously dispersed periodic fibers are obtained with a random sequential adsorption algorithm described in Appendix C. In the simulations, fiber volume fractions up to 15% (approximately 22000 fibers) are considered. Two sample distributions with approximately 4700 aligned and randomly distributed discrete fibers are shown in Fig. 16 yielding composites with transversely isotropic and nearly isotropic mechanical responses.

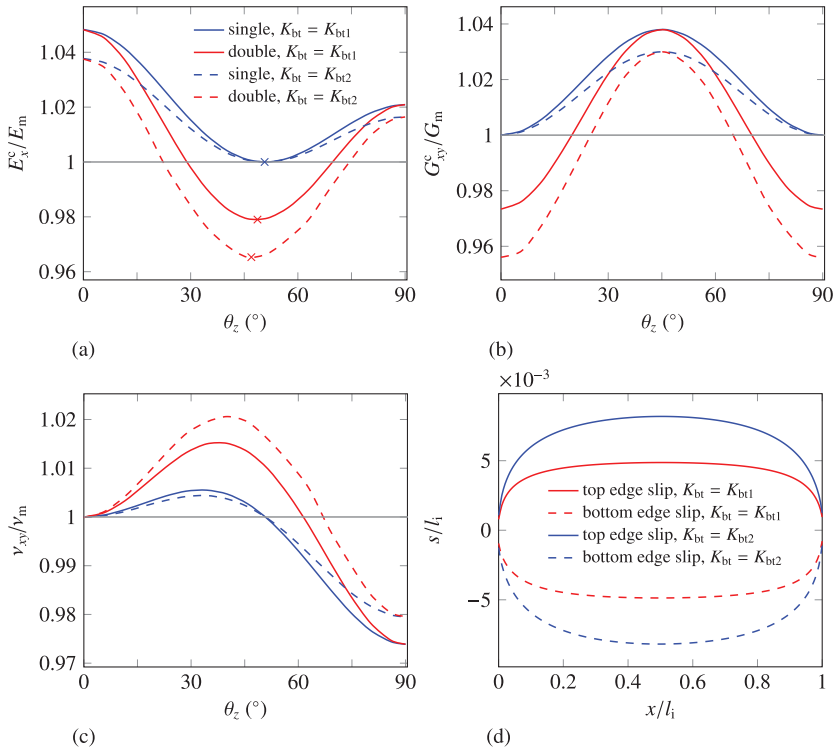

Fig. 15. Effective (a) Young's modulus, (b) shear modulus and (c) Poisson's ratios of a two-dimensional composite with imperfect interface ($K_{bt1} = 1000$ N/mm^2, $K_{bt2} = 500$ N/mm^2, $E_f/E_m = 10$ and $\nu_m = 0.4$ in plane strain). The single-interface model shows neutrality for $\theta = \theta_n$ ($\theta_n \approx 50.7°$ from Fig. 7b), while the double-interface model predicts degraded effective mechanical properties compared with intact matrix properties. (d) Fiber interfacial slips for $\theta = \theta_n$ using the double-interface model. (For interpretation of the references to colour in this figure legend, the reader is referred to the web version of this article.)

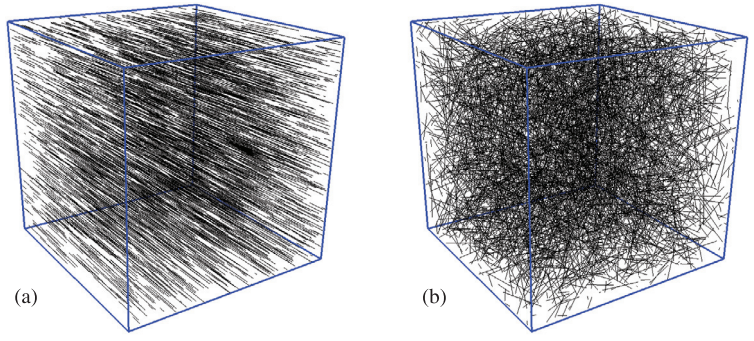

Fig. 16. Two realizations of a composite with approximately 4700 fiber (length $l_f = 0.2L$ and diameter $d_f = 0.007L$) in an $L \times L \times L$ ($L = 1$ mm) periodic simulation box resulting in a fiber volume fraction $v_f = 3\%$: (a) aligned and (b) randomly distributed fibers.

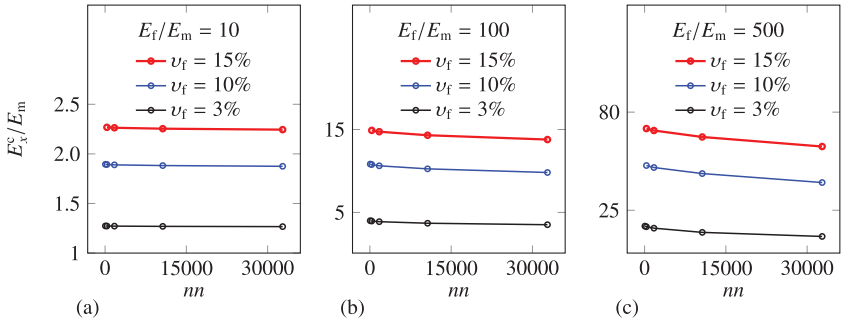

Fig. 17. Effective Young's modulus along the x-axis for a transversely isotropic composite with aligned fibers for different mesh densities (nn indicates the number of mesh nodes) and fiber volume fractions v_f. In the calculations reported in Section 5 ($d_f = 0.007L$ and $l_f = 0.2L$), the finest discretization with $31 \times 31 \times 31$ trilinear hexahedral elements and 32768 nodes has been used.

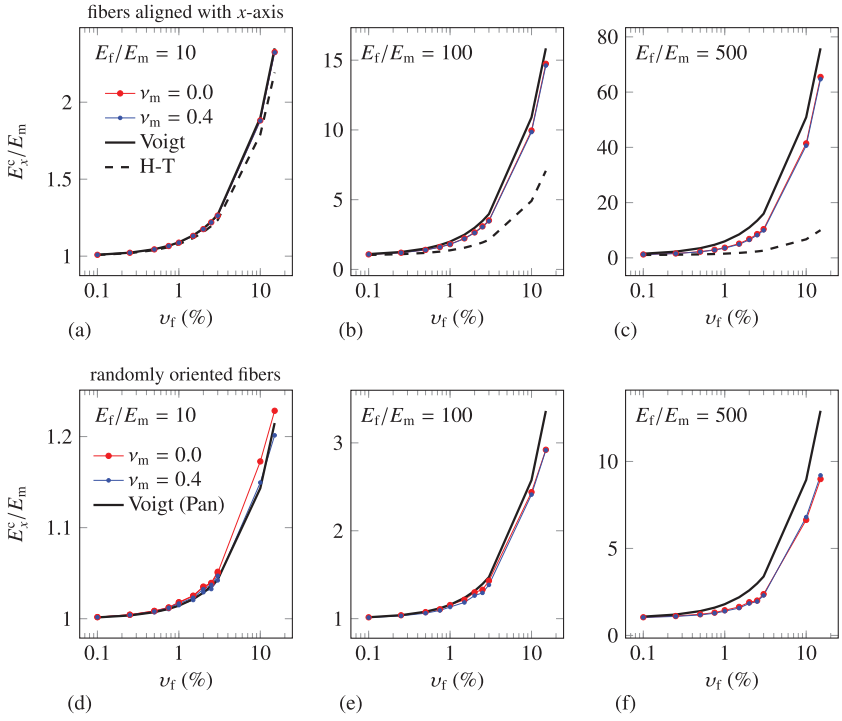

Fig. 18. Effective Young's modulus along the x-axis for a transversely isotropic composite with aligned fibers (a-c) and a nearly isotropic composite with randomly distributed fibers (d-f) at different fiber volume fractions υ_f ($d_f = 0.007L$ and $l_f = 0.2L$).

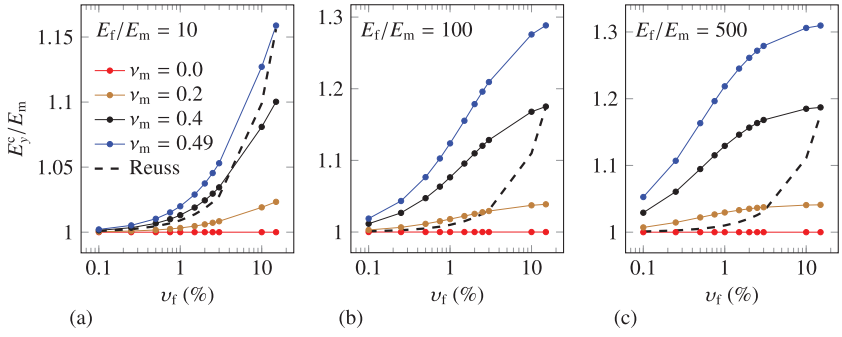

Fig. 19. Effective transverse Young's moduli ($E_y^c = E_z^c$) for a transversely isotropic composite with aligned fibers at different volume fractions υ_f ($d_f = 0.007L$ and $l_f = 0.2L$).

Young's moduli. Fig. 18 shows the homogenized Young's modulus E_x^c as a function of the fiber volume fraction υ_f for different material properties and distributions of fibers; in the figure, numerical results are compared with rule-of-mixtures (RoM) and Halpin–Tsai estimates. As shown in Figs. 18a–c for a transversely isotropic composite, due to the slenderness of the fibers (aspect ratio $l_f/d_f \approx 30$), numerical results are generally in better agreement with RoM predictions especially for fibers with relatively low Young's modulus. The longitudinal Young's modulus increases with the fiber volume fraction υ_f and is hardly influenced by the matrix Poisson's ratio ν_m. Although a similar pattern is observed in Figs. 18d–f for randomly distributed fibers, the resulting Young's moduli are significantly lower due to fiber orientation with respect to the loading direction and are in good agreement with the simple modified Voigt estimate provided by Pan (1996).

In a transversely isotropic composite similar to that in Fig. 16a, Young's moduli E_y^c and E_z^c ($= E_y^c$) are also enhanced for a matrix material with non-zero Poisson's ratio. However, as shown in Fig. 19, the value of the transverse Young's modulus does not generally agree with RoM estimates and this is attributed to the unrealistic uniform stress assumption and the absence of Poisson's contraction effects (Hull and Clyne, 1996). For a nearly incompressible matrix, RoM predictions clearly underestimate the transverse Young's moduli of the transversely isotropic composite.

Poisson's ratios. Fig. 20 shows the effective Poisson's ratios of the transversely isotropic composite for various fiber volume fractions. Similar to the transverse Young's moduli, Poisson's ratio $\nu_{zy}^c (= \nu_{yz}^c)$ shows an increasing trend and a considerable dependence on the matrix Poisson's ratio. This dependence however is not predicted by RoM estimates, which clearly overestimates the numerical results. Conversely, $\nu_{yx}^c (= \nu_{zx}^c)$ decreases, in good agreement with RoM, and the results are not influenced by the matrix Poisson's ratio. Finally, as shown in Fig. 20c (and already reported in Fig. 9c for a fixed volume fraction with $\theta_z = 0^\circ$), ν_{xy}^c ($= \nu_{xz}^c$) remains equal to the matrix Poisson's ratio irrespective of fiber density, a property which is not predicted by RoM estimates (Eq. (B.5)).

Figs. 21 and 22 show results for the homogenized effective Poisson's ratio of the nearly isotropic composite as a function of ν_m and υ_f. Values of the effective Poisson's ratio

$$\nu_{iso}^c = \frac{\lambda^c}{2(\mu^c + \lambda^c)}, \tag{19}$$

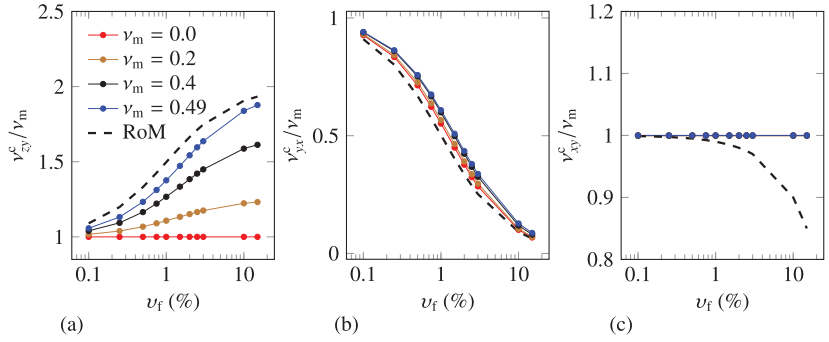

Fig. 20. Effective Poisson's ratios of a transversely isotropic composite with aligned fibers for different volume fractions ($E_f/E_m = 100$, $d_f = 0.007L$ and $l_f = 0.2L$).

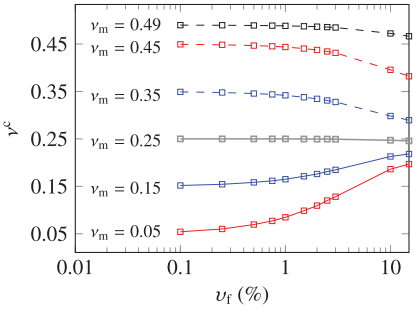

Fig. 21. Effective Poisson's ratios ν^c_{iso} of a nearly isotropic composite with randomly distributed fibers for different volume fractions υ_f (matrix Poisson's ratios ν_m, $E_f/E_m = 100$, $d_f = 0.007L$ and $l_f = 0.2L$).

where λ^c and μ^c are the effective Lamé parameters averaged in the three directions, are computed assuming an isotropic behavior of the composite (Nemat-Nasser and Hori, 1998). From Fig. 21, it is interesting to notice that for a matrix with Poisson's ratio $\nu_m \approx 0.25$, the effective Poisson's ratio ν^c_{iso} of the homogenized composite is insensitive to the fiber volume fraction (the inclusions are neutral in terms of Poisson's ratio). For $\nu_m < 0.25$, an increased incompressibility of the composite is observed; for a matrix with $\nu_m > 0.25$, an increased compressibility, although less pronounced than the increase in incompressibility, is observed. In both cases, values of the effective Poisson's ratio tends toward the value 0.25 by increasing the fiber volume fraction υ_f. As shown in Fig. 22 for different fiber stiffnesses, a similar observation can be made in terms of the mean anisotropic Poisson's ratios ν^c_a (averaged over anisotropic Poisson's ratios ν_{xy}, ν_{xz}, ν_{yx}, ν_{zx}, ν_{zy} and ν_{yz}, from Eq. (A.2)). Due to the random distribution of the fibers, anisotropic Poisson's ratios only slightly deviate from the mean value. These observations are in agreement with previous findings by Das and MacKintosh (2010) who used a mean-field approach for the theoretical investigation of the micromechanics of isotropic composites consisting of randomly distributed stiff fibers. By taking into account the reinforcing effect of individual fibers, the current numerical homogenization procedure validates averaging theories and neutrality in terms of Poisson's ratio for a composite with randomly distributed linear elastic fibers embedded in a matrix with Poisson's ratio $\nu_m = 0.25$ or a nearly incompressible matrix with $\nu_m \approx 0.5$.

Unlike mean-field homogenization, embedded reinforcement methods are not limited to composites with perfect matrix-fiber

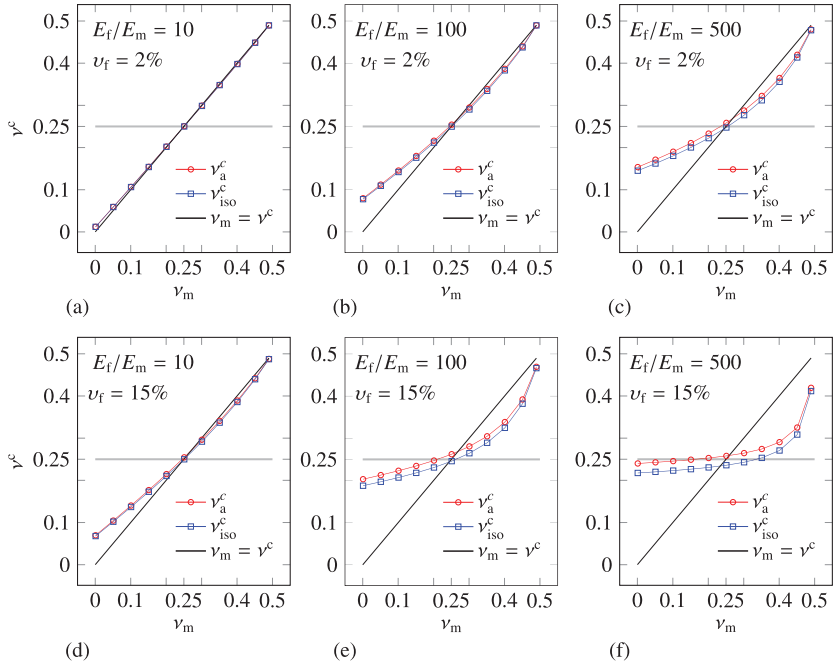

Fig. 22. Effective Poisson's ratio of a nearly isotropic composite with randomly distributed fibers at two volume fractions υ_f and different matrix Poisson's ratios ν_m, with $d_f = 0.007L$ and $l_f = 0.2L$.

interfaces. Various distribution of fibers with arbitrary shapes and interface properties can be considered for the evaluation of the composite homogenized mechanical properties.

6. Concluding remarks

It is well known that fiber orientation plays an important role in the mechanical response of composites. The common understanding is that fibers improve the mechanical properties of the matrix in which they are embedded, and that certain fiber orientations are better than others in some measure. This is not correct. The most unfavorable fiber orientation represents a state of fiber neutrality, a situation in which a fiber does not perturb the stress field and therefore has no influence on the mechanical properties of the composite. Fiber neutrality can be seen as the generalization of the concept of inclusion neutrality that was introduced for zero-thickness rigid inclusions by Wang et al. (1985). Here, we have demonstrated that inclusion neutrality holds also for thin linear elastic fibers with imperfect matrix-fiber interfaces, with an immediate generalization to the perfect interface case.

Similar to rigid line inclusions, slenderness is a fundamental ingredient for the occurrence of neutrality. Neutral fibers are in fact not reported in existing studies where composites with relatively large fiber diameters were studied. In these cases the effective stiffness of the composite increases even though fibers are oriented at the most unfavorable angle—this angle would result in fiber neutrality if the fiber were thin.

Acknowledgments

The research leading to these results has received funding from the European Research Council under the European Union's Seventh Framework Programme (FP7/2007-2013) / ERC Grant agreement no. 617972.

Appendix A. Computation of effective properties

To extract the effective elastic coefficients of the fiber-reinforced composite, we employ the computational homogenization scheme described by Berger et al. (2005). As suggested by Xia et al. (2003), homogeneous boundary conditions lead to over-constrained predictions of the effective properties. Instead, the periodic boundary conditions

$$u_i^k - u_i^l = \bar{\varepsilon}_{ij} L_j, \tag{A.1}$$

prescribed at the boundary of the simulation box with $\bar{\varepsilon}_{ij}$ $(i, j = x, y, z)$ the components of the applied strain tensor, yield more accurate estimations. Edge indexes k and l correspond to two opposite edges of the simulation box where periodic strains are imposed, and L_j is the size of the domain in the jth direction. In all the numerical results presented in this paper, a unit cube simulation box is adopted (Fig. 3).

Although 21 independent constants are defined for the general anisotropic case (Nemat-Nasser and Hori, 1998), here only the specific engineering constants in each direction are of interest. Three Young's moduli (E_x^c, E_y^c, E_z^c) relating tensile stresses and strains, three shear moduli (G_{xy}^c, G_{yz}^c, G_{xz}^c) relating shearing stresses and strains, and six Poisson's ratios ν_{ij}^c (ν_{xy}^c, ν_{xz}^c, ν_{yx}^c, ν_{yz}^c, ν_{zx}^c, ν_{zy}^c) representing contraction in the j-direction after the application of a tensile load in the i-direction can be extracted. These quantities may be expressed in terms of the coefficients of the compliance constants matrix as

$$E_x^c = \frac{1}{C_{11}},\ E_y^c = \frac{1}{C_{22}},\ E_z^c = \frac{1}{C_{33}},$$
$$G_{xy}^c = \frac{1}{C_{44}},\ G_{yz}^c = \frac{1}{C_{55}},\ G_{xz}^c = \frac{1}{C_{66}},$$
$$\nu_{xy}^c = -\frac{C_{21}}{C_{11}},\ \nu_{xz}^c = -\frac{C_{31}}{C_{11}},$$
$$\nu_{yx}^c = -\frac{C_{12}}{C_{22}},\ \nu_{yz}^c = -\frac{C_{32}}{C_{22}},$$
$$\nu_{zx}^c = -\frac{C_{13}}{C_{33}},\ \nu_{zy}^c = -\frac{C_{23}}{C_{33}}. \tag{A.2}$$

The compliance constants matrix $\boldsymbol{C}$ is evaluated by inverting the elastic coefficient matrix $\boldsymbol{D}$ as described in Malagù et al. (2017).

Appendix B. Analytical micromechanical models

For the special case of a transversely isotropic composite with aligned fibers of the type shown in Fig. 16a, simple analytical micromechanical models are available.

The well known rule of mixtures is widely used to predict the mechanical properties of elastic composites. The composite stiffness is approximated as a weighted mean of the moduli of two components (Hull and Clyne, 1996). The rule of mixtures does not consider geometrical details such as the fiber aspect ratio. With reference to the case of a composite with fibers that are aligned with the global x-axis, the effective longitudinal Young's modulus

$$E_x^c = (1 - \upsilon_f)\, E_m + \upsilon_f E_f \tag{B.1}$$

is expressed as a function of the fiber volume fraction υ_f, where it is assumed that strains in the direction of the fibers are equal in the matrix and the fiber (this assumption is valid for perfectly bonded fibers with high aspect ratio). Eq. (B.1) is referred to as the upper bound modulus (Voigt model).

Using the inverse rule of mixtures and assuming that stresses in the direction normal to the fibers are equal in the matrix and the fiber, the transverse Young's moduli

$$E_y^c = E_z^c = \left[\frac{\upsilon_f}{E_f} + \frac{1 - \upsilon_f}{E_m}\right]^{-1}. \tag{B.2}$$

This expression is known as the lower-bound modulus (Reuss model).

According to the semi-empirical estimate of the Young's modulus proposed by Halpin (1969),

$$E_x^c = E_m \frac{1 + \xi \eta \upsilon_f}{1 - \eta \upsilon_f} \tag{B.3}$$

with

$$\eta = \frac{E_f/E_m - 1}{E_f/E_m + \xi} \quad \text{and} \quad \xi = 2l_f/d_f. \tag{B.4}$$

This expression is suitable for short fibers and takes into account the non-uniform distribution of strains and stresses in the composite. Predictions of Eq. (B.3) lie within the range of the lower and upper bound moduli.

Similar formulas can be derived for the Poisson's ratios (Hull and Clyne, 1996):

$$\nu_{xy}^c = (1 - \upsilon_f)\, \nu_m + \upsilon_f \nu_f,$$
$$\nu_{yx}^c = [(1 - \upsilon_f)\, \nu_m + \upsilon_f \nu_f]\frac{E_y}{E_x}, \text{ and}$$
$$\nu_{yz}^c = 1 - \nu_{yx} - \frac{E_y}{3K} \quad \text{with} \quad K = \left[\frac{\upsilon_f}{K_f} + \frac{1 - \upsilon_f}{K_m}\right]^{-1}, \tag{B.5}$$

where K_m and K_f are the bulk moduli of the constituents.

For a composite with randomly distributed fibers with isotropic behavior, the simple rule of mixtures estimate yields

$$E_{x,y,z}^c = \left(1 - \frac{\upsilon_f}{2\pi}\right) E_m + \frac{\upsilon_f}{2\pi} E_f, \tag{B.6}$$

where a probability density function is used to specify the random fiber orientation as proposed by Pan (1996).

Appendix C. Generation of periodic simulation box

For the generation of periodic fiber distributions in the simulation box, the random sequential adsorption algorithm (Kari et al., 2007) was implemented. Starting with a box of certain dimensions and knowing the volume fraction, length and diameter of the fibers, for each fiber the coordinates of one end point is determined using the Matlab® rand function. Orientation of the fiber is fixed for aligned fibers, while for the randomly distributed fibers, the orientation is determined using the rand function. Having the fiber orientation and coordinates of one fiber end point, the coordinates of the second point are determined. If the new point lies outside the simulation box, the out of box segment of the fiber is cut and moved to the opposite boundary to preserve periodicity. This process is repeated for all fibers consecutively until the desired volume fraction is achieved.

References

Andrews, R., Jacques, D., Minot, M., Rantell, T., 2002. Fabrication of carbon multiwall nanotube/polymer composites by shear mixing. Macromol. Mater. Eng. 287 (6), 395–403.

Balakrishnan, S., Murray, D.W., 1986. Finite element prediction of reinforced concrete behavior. Structural Engineering Report No. 138. Department of Civil Engineering, University of Alberta, Edmonton, Alberta, Canada.

Barbieri, E., Pugno, N.M., 2015. A computational model for large deformations of composites with a 2D soft matrix and 1D anticracks. Int. J. Solids Struct. 77, 1–14.

Barzegar, F., Maddipudi, S., 1997. Three-dimensional modeling of concrete structures. II: reinforced concrete. J. Struct. Eng. 123 (10), 1347–1356.

Benveniste, Y., Miloh, T., 1999. Neutral inhomogeneities in conduction phenomena. J. Mech. Phys. Solids 47 (9), 1873–1892.

Berger, H., Kari, S., Gabbert, U., Rodriguez-Ramos, R., Guinovart, R., Otero, J.A., Bravo–Castillero, J., 2005. An analytical and numerical approach for calculating effective material coefficients of piezoelectric fiber composites. Int. J. Solids Struct. 42 (21), 5692–5714.

Budiansky, B., Fleck, N.A., 1993. Compressive failure of fibre composites. J. Mech. Phys. Solids 41 (1), 183–211.

Dal Corso, F., Shahzad, S., Bigoni, D., 2016. Isotoxal star-shaped polygonal voids and rigid inclusions in nonuniform antiplane shear fields. Part II: Singularities, annihilation and invisibility. Int. J. Solids Struct. 85, 76–88.

Das, M., MacKintosh, F.C., 2010. Poisson's ratio in composite elastic media with rigid rods. Phys. Rev. Lett. 105 (13), 138102.

Duflot, M., 2006. A meshless method with enriched weight functions for three-dimensional crack propagation. Int. J. Numer. Methods Eng. 65 (12), 1970–2006.

Durand, R., Farias, M.M., Pedroso, D.M., 2015. Computing intersections between non-compatible curves and finite elements. Comput. Mech. 56 (3), 463–475.

Elwi, A.E., Hrudey, T.M., 1989. Finite element model for curved embedded reinforcement. J. Eng. Mech. 115 (4), 740–754.

Hall, L.J., Coluci, V.R., Galvão, D.S., Kozlov, M.E., Zhang, M., Dantas, S.O., Baughman, R.H., 2008. Sign change of Poisson's ratio for carbon nanotube sheets. Science 320 (5875), 504–507.

Halpin, J.C., 1969. Effects of Environmental Factors on Composite Materials. Technical Report. AFML-TR 67-423.

Hartl, H., 2002. Development of a Continuum-Mechanics-Based Tool for 3D Finite Element Analysis of Reinforced Concrete Structures and Application to Problems of Soil-Structure Interaction. Graz University of Technology, Austria (PhD thesis).

Hull, D., Clyne, T.W., 1996. An Introduction to Composite Materials. Cambridge University Press.

Kang, G.Z., Gao, Q., 2002. Tensile properties of randomly oriented short $\delta-Al_2O_3$ fiber reinforced aluminum alloy composites: II. Finite element analysis for stress transfer, elastic modulus and stress-strain curve. Compos. Part A 33 (5), 657–667.

Kari, S., Berger, H., Gabbert, U., 2007. Numerical evaluation of effective material properties of randomly distributed short cylindrical fibre composites. Comput. Mater. Sci. 39 (1), 198–204.

Lusti, H.R., Gusev, A.A., 2004. Finite element predictions for the thermoelastic properties of nanotube reinforced polymers. Modell. Simul. Mater. Sci. Eng. 12 (3), S107.

Malagù, M., Goudarzi, M., Lyulin, A., Benvenuti, E., Simone, A., 2017. Diameter-dependent elastic properties of carbon nanotube-polymer composites: Emergence of size effects from atomistic-scale simulations. Compos. Part B 131, 260–281.

Mortazavi, B., Baniassadi, M., Bardon, J., Ahzi, S., 2013. Modeling of two-phase random composite materials by finite element, Mori–Tanaka and strong contrast methods. Compos. Part B 45 (1), 1117–1125.

Nemat-Nasser, S., Hori, M., 1998. Micromechanics: Overall Properties of Heterogeneous Materials. Elsevier.

Ninić, J., Stascheit, J., Meschke, G., 2014. Beam-solid contact formulation for finite element analysis of pile-soil interaction with arbitrary discretization. Int. J. Numer. Anal. Methods Geomech. 38 (14), 1453–1476.

Noselli, G., Dal Corso, F., Bigoni, D., 2010. The stress intensity near a stiffener disclosed by photoelasticity. Int. J. Fract. 166 (1), 91–103.

Pan, N., 1996. The elastic constants of randomly oriented fiber composites: A new approach to prediction. Sci. Eng. Compos. Mater. 5, 63–72.

Pierard, O., Friebel, C., Doghri, I., 2004. Mean-field homogenization of multi-phase thermo-elastic composites: A general framework and its validation. Compos. Sci. Technol. 64 (10-11), 1587–1603.

Pike, M.G., Hickman, M.A., Oskay, C., 2015. Interactions between multiple enrichments in extended finite element analysis of short fiber reinforced composites. Int. J. Multiscale Comput. Eng. 13 (6), 507–531.

Pike, M.G., Oskay, C., 2016. Three-dimensional modeling of short fiber-reinforced composites with extended finite-element method. J. Eng. Mech. 142 (11), 04016087.

Radtke, F.K.F., Simone, A., Sluys, L.J., 2010. A partition of unity finite element method for obtaining elastic properties of continua with embedded thin fibres. Int. J. Numer. Methods Eng. 84 (6), 708–732.

Ru, C.Q., 1998. Interface design of neutral elastic inclusions. Int. J. Solids Struct. 35 (7–8), 559–572.

Sheng, N., Boyce, M.C., Parks, D.M., Rutledge, G.C., Abes, J.I., Cohen, R.E., 2004. Multiscale micromechanical modeling of polymer/clay nanocomposites and the effective clay particle. Polymer 45 (2), 487–506.

Tian, W., Qi, L., Su, C., Zhou, J., Jing, Z., 2016. Numerical simulation on elastic properties of short-fiber-reinforced metal matrix composites: Effect of fiber orientation. Compos. Struct. 152, 408–417.

Tian, W., Qi, L., Zhou, J., Guan, J., 2014. Effects of the fiber orientation and fiber aspect ratio on the tensile strength of C_{sf}/Mg composites. Comput. Mater. Sci. 89, 6–11.

Wang, Z.Y., Zhang, H.T., Chou, Y.T., 1985. Characteristics of the elastic field of a rigid line inhomogeneity. J. Appl. Mech. 52 (4), 818–822.

Xia, Z., Zhang, Y., Ellyin, F., 2003. A unified periodical boundary conditions for representative volume elements of composites and applications. Int. J. Solids Struct. 40 (8), 1907–1921.